

Discovery of a large magnetic nonlinear Hall effect in an altermagnet

Lei Han^{1,†}, Xizhi Fu^{2,†}, Cheng Song^{1,*}, Yuxiang Zhu¹, Xiaokang Li³, Zengwei Zhu³, Hua Bai¹, Ruiyue Chu¹, Jiankun Dai¹, Shixuan Liang¹, Junwei Liu^{2,*}, Feng Pan^{1,*}

¹Key Laboratory of Advanced Materials (MOE), School of Materials Science and Engineering, Tsinghua University, Beijing 100084, China.

²Department of Physics, The Hong Kong University of Science and Technology, Hong Kong 999077, China.

³Wuhan National High Magnetic Field Center and School of Physics, Huazhong University of Science and Technology, Wuhan 430074, China.

*Corresponding author. Email: songcheng@mail.tsinghua.edu.cn; liuj@ust.hk; panf@mail.tsinghua.edu.cn.

†These authors contributed equally.

Abstract

Since Edwin Hall's groundbreaking discovery of the Hall effect in 1879, magnetism, spin, and quantization have been expanding the scope of Hall effects, continuously driving transformative progress in science and technology. Among them, the latest nonlinear Hall effect (NLHE), where longitudinal electric field tunes quantum geometry to generate nonlinear Hall voltage, attracts wide attention as a sensitive probe of topological phases across a wide range of materials. Here, we report a new Hall effect member: the magnetic nonlinear Hall effect (MNLHE), characterized by a quadratic Hall conductivity dependence on magnetic field—rather than electric field as in NLHE. This finding relies on an altermagnet, Mn_5Si_3 thin film, whose alternating-sign Berry curvatures ensure higher-order MNLHE clearly distinguishable from the first-order anomalous Hall effect. The observed quadratic dependence originates from chiral next-nearest-neighbor hopping processes that acquire magnetic-exchange-driven Zeeman energies and Haldane-like chiral flux phases. Remarkably, this MNLHE is non-analytic, as reversing the magnetic field

flips the alternating spin-splitting bands and reverses the hopping chirality, which is absent in traditional NLHE. Beyond offering a distinctive transport fingerprint for altermagnet Mn_5Si_3 thin film, this MNLHE is large and unsaturated up to 60 T, providing opportunities for pulsed high-field sensing technologies in both fundamental researches and engineering applications.

Main

The ordinary Hall effect is one of the oldest phenomena¹ in condensed matter physics, and over the past few decades, it is hard to overemphasize the impact of the milestone advancements in new Hall effects on the field.²⁻⁷ Discoveries like the anomalous⁷, spin⁶, and quantum Hall effect² are far more than novel phenomena—they serve as defining tools for uncovering fundamental insights into Fermi surface features, spin-orbit coupling, and topological physics, while driving groundbreaking applications like precise sensing, low-power spintronics, and quantum computing. Recently, nonlinear Hall effects (NLHEs)^{8,9}, i.e., higher-order Hall responses to longitudinal electric field (Fig. 1a), have garnered wide attention as highly sensitive probes of topological phases and quantum geometry across a broad range of materials like 2D materials⁹⁻¹⁴, twisted systems^{15,16}, and Weyl/Dirac semimetals¹⁷⁻²¹.

Typically, NLHEs arise from electric field modulation of quantum geometry, and thus these electric-field-relevant NLHEs are referred to as ENLHEs here. For instance, as shown in Fig. 1b and 1c, bands connected by time-reversal symmetry (T), i.e., T -paired spin-valley locking (TSVL)²², exhibit opposite Berry curvatures (in red and blue), with the black circle marking the original Fermi surface and the red/blue circles indicating the electric-field-tilted Fermi surfaces. Berry curvature dipole⁸/quadruple²³ emerge due to Fermi surface tilting, which generate second-order⁹/third-order²⁴ ENLHEs. Despite showcasing the elegance of inversion symmetry (P) breaking,²⁵ these ENLHEs remain inherently weak. Thus, direct measurement of DC nonlinear Hall voltage under a DC electric field is challenging; instead, AC fields E_{AC} combined with lock-in amplifiers are required to detect the AC higher-order Hall voltage V_{AC} , as shown in Fig. 1a.

Magnetic field can also modulate Berry curvature to generate NLHE²⁶, termed magnetic nonlinear Hall effects (MNLHE) as a new Hall effect (Fig. 1d), as their mechanisms are essentially distinct from ENLHEs. Crucially, magnetic field may offer far stronger modulation for detectable DC nonlinear Hall voltage, as it both induces Zeeman band shifts and tunes the order parameter of magnetic materials. However, MNLHE have been remaining unreported for long. Note that in some P broken systems, the second-order Hall resistance can be linearly dependent on both electric field and magnetic field, i.e., the bilinear magnetoelectric resistance^{27,28}. Such phenomena are relevant to magnetic-field-dependent charge-spin interconversion process instead of magnetic-field-modulated Berry curvature. It is challenging to observe MNLHE due to inherent limitations of traditional magnetic materials. They either exhibit single-sign Berry curvature, as in ferromagnets, where the dominant first-order effects like anomalous Hall effect (AHE) overshadow higher-order MNLHEs, or retain PT symmetry, as in conventional antiferromagnets, suppressing Berry curvature and inhibiting large MNLHEs.

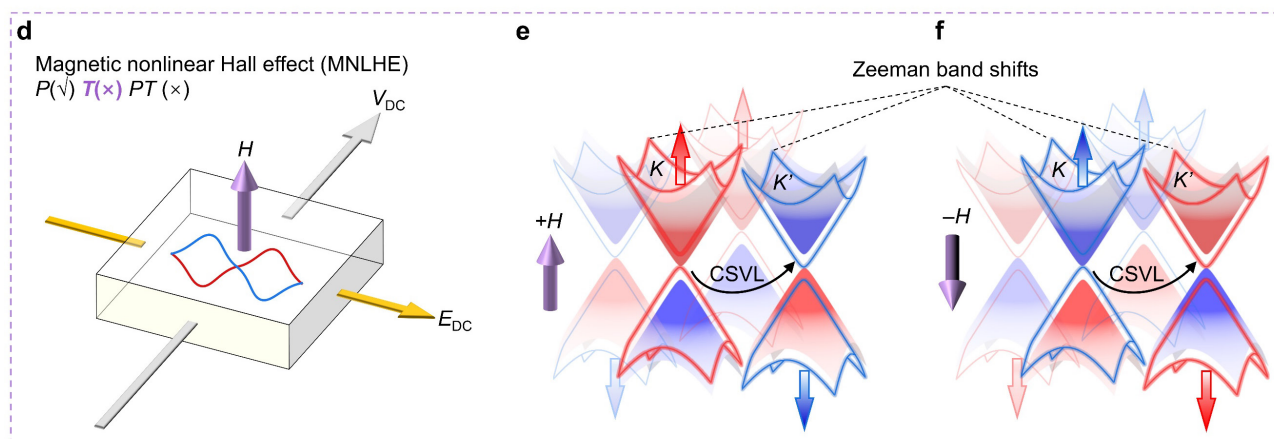
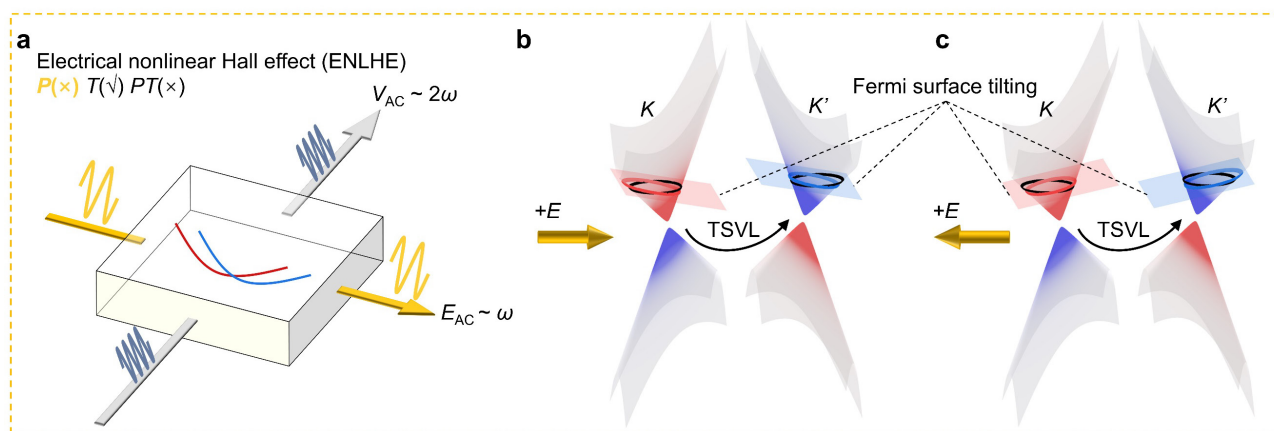


Figure 1 | Comparison of ENLHE and MNLHE. (a) Schematic of ENLHE in materials with P symmetry breaking, showing Rashba spin-splitting bands (red and blue lines). Second-order ENLHE is illustrated here, where a longitudinal AC electric field E_{AC} with frequency ω generates a nonlinear Hall voltage V_{AC} at 2ω , detectable via lock-in amplifiers. (b, c) Band, Berry curvature and Fermi surface modulation under opposite electric fields for ENLHE. Bands are connected by TSVL, with red and blue indicating opposite Berry curvatures. Black and red/blue circles represent the Fermi surface without and with the electric field modulation, respectively. (d) Schematic for MNLHE in altermagnet with T symmetry breaking, showing alternating spin-splitting bands (red and blue lines). DC nonlinear Hall voltage V_{DC} is detectable under a DC longitudinal electric field E_{DC} . (e, f) Bands and Berry curvature modulation under opposite magnetic fields for MNLHE in an altermagnet. Bands connected by CSVL of C_4T are shown as an example. Red and blue in the bands represent opposite Berry curvatures, with the color of contours denoting opposite spins. Zeeman shifts of these bands under magnetic field are shown by the shift of these contours.

Altermagnets^{29,30} (AMs) present an ideal platform for observing MNHLEs. Characterized by alternating collinear compensated magnetic moments in real space³¹ and alternating spin-splitting bands in momentum space³², AMs break PT symmetry while preserve C -paired spin valley locking (CSVL)²². This generates non-zero but alternating-sign Berry curvature $\mathbf{\Omega}$ at CSVL \mathbf{k} -points ($C\mathbf{\Omega} = -\mathbf{\Omega}$), where C is C_4T as an example shown in Fig. 1e and 1f. Alternating-sign Berry curvature suppresses strong first-order Hall responses³³⁻³⁷, as PT symmetry breaking in altermagnets is in fact intrinsically tied to higher-order Hall effects^{38,39}, thereby making higher-order MNHLEs distinguishable. Meanwhile, an external magnetic field can induce a Zeeman shift in the CSVL bands of AMs (Fig. 1e and 1f, denoted by the red and blue contours) to break the $C\mathbf{\Omega} = -\mathbf{\Omega}$ relationship, while simultaneously tunes the order parameter to modulate $\mathbf{\Omega}$, significantly enhancing net $\mathbf{\Omega}$ near the Fermi surface. Therefore, AMs not only create opportunities for large MNHLEs but also, in turn,

establish MNHLE as a promising AM's fingerprint by offering deeper insights into spin-splitting bands and Berry curvature, which represents an urgent but unexplored research direction.

Herein, we report the discovery of a large MNHLE in epitaxially strained Mn_5Si_3 thin film, an AM candidate, which can be directly measured by DC Hall voltage and does not saturate even up to ~ 60 T. The terminology of MNLHE is to emphasize its fundamental difference from ENLHE. MNLHE is characterized by a quadratic dependence of Hall conductivity on magnetic field due to chiral next-nearest-neighbor (NNN) hopping, reminiscent of the Haldane model with chiral flux phases. The reversal of hopping chirality under magnetic field produces unique non-analytic feature, which is originated in the flipping of spin-splitting bands and absent in ENLHE. Beyond its scientific significance, the large and unsaturated MNLHE is highly promising for high-field sensing in applications such as plasma science, condensed matter physics, magnetic flux compression, or magnetic pulse welding.

Experimental observation of non-analytic quadratic Hall conductivity with magnetic field

Mn_5Si_3 thin films are chosen due to their paramagnet (PM)-to-AM and AM-to-noncollinear AFM (ncAFM) phase transitions, enabling *in-situ* comparisons of Hall responses in these phases.^{35,36,40} As shown latter, these comparisons allow us to effectively exclude possible nonlinearity in Hall response due to multi-carrier effect, like in CrSb.⁴¹⁻⁴³ In each Mn_5Si_3 unit cell, four Mn_a and six Mn_b occupy two inequivalent Wyckoff positions (Fig. 2a). As the temperature drops into the AM phase, G-type AFM ordering develops on four of the six Mn_b atoms in two atomic layers at $z = 1/4$ and $z = 3/4$ (green planes in Fig. 2a), forming the Néel vector n as the order parameter. In bulk Mn_5Si_3 , the PM-to-AM magnetic phase transition is accompanied by the hexagonal-to-orthorhombic structural transition, with the resulting orthorhombic structure conserving PT and tT symmetry.^{44,45} In contrast, for Mn_5Si_3 thin film, this hexagonal-to-orthorhombic transition is suppressed due to strain, breaking PT and tT symmetry and making strained Mn_5Si_3 thin film an AM.^{35,36,46}

Experimentally, 100 nm $\text{Mn}_5\text{Si}_3(0001)$ thin film grown on the $\text{Al}_2\text{O}_3(0001)$ substrate follows the epitaxial relationship of $\text{Al}_2\text{O}_3(0001)[01\bar{1}0]/\text{Mn}_5\text{Si}_3(0001)[11\bar{2}0]$, and undergoes PM-to-AM and AM-to-ncAFM magnetic phase transitions at 63 K and 243 K, respectively (Methods, Extended Data Fig. 1). A weak-field (1.5 T) AHE and tiny strain-induced spontaneous canting moment m of $\sim 2 \text{ emu cc}^{-1}$ are observed, agree with previous studies.^{35,46} Due to symmetry, m allows first-order linear anomalous Hall responses, e.g., AHE^{35,36,40}, anomalous Nernst effect^{46,47}, and magneto-optical Kerr effect.³⁵ Crucially, it is the Berry curvature determined by n instead of tiny m that dominates these responses.

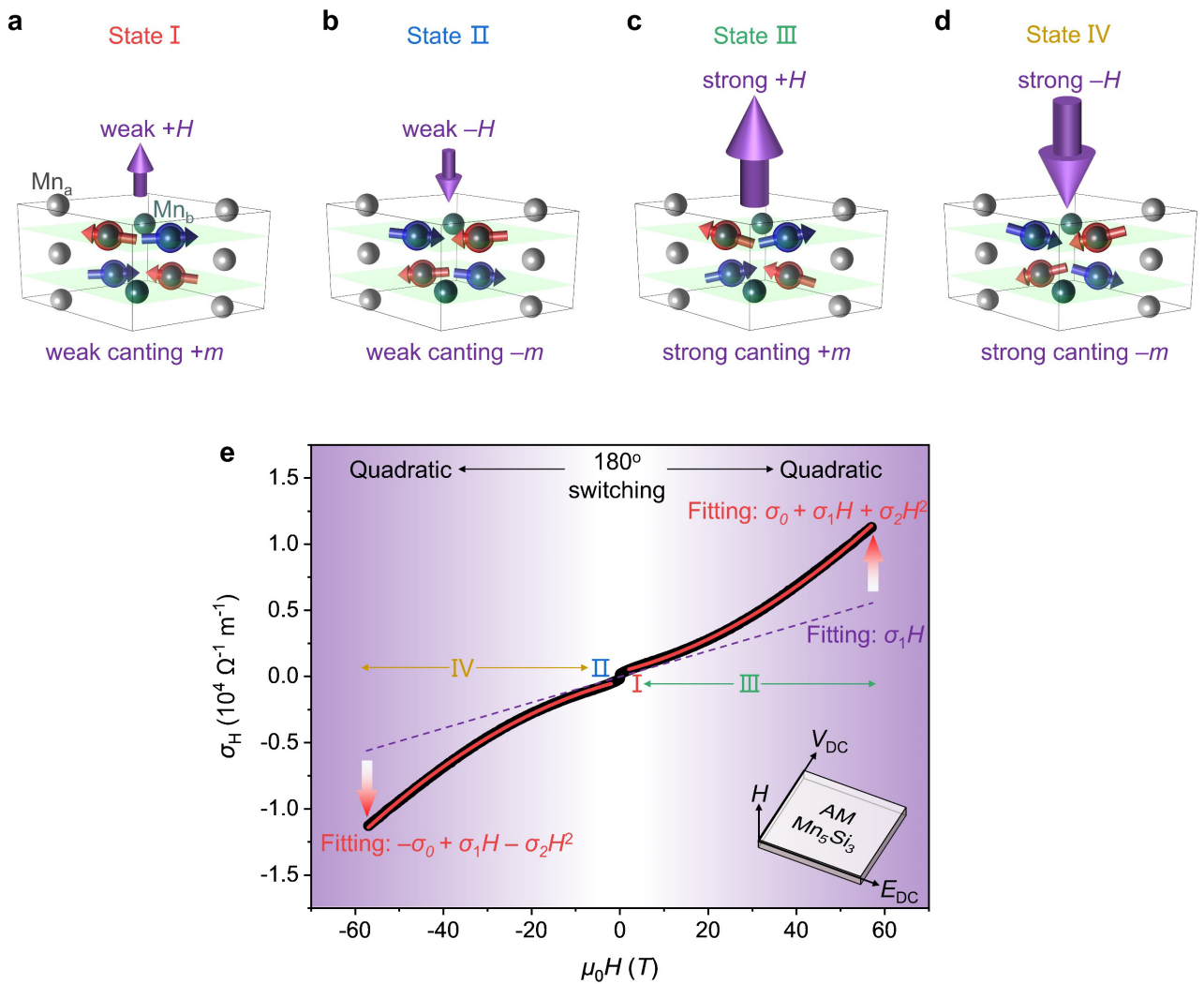


Figure 2 | Experimental observation of a large MNLHE. (a-d) Schematic illustrations of the four magnetic states I-IV under strong or weak magnetic field applied in opposite directions. Only Mn atoms of the Mn_5Si_3 unit cell are shown for clarity. (e) Hall conductivity σ_H measured under a

perpendicular magnetic field (solid black line) in 100 nm Mn₅Si₃(0001) thin film. A gradient background illustrates the smooth evolution from a regime dominated by the AHE due to 180° magnetic structure switching to one characterized by a $\text{sgn}(H)\sigma_2H^2$ term. The dashed purple and solid red lines denote fitting results using $\sigma_H = \sigma_1H$ and $\sigma_H = \text{sgn}(H)\sigma_0 + \sigma_1H + \text{sgn}(H)\sigma_2H^2$, respectively.

As we discussed in Fig. 1e and 1f, magnetic field H induces Zeeman bands shifts to tune the Berry curvature near the Fermi surface. Next, we discuss the change of order parameter under H , which may directly change the Berry curvature itself. Under a weak magnetic field H (~ 1 T), m can be switched by 180°, simultaneously driving the 180° switching of n (Fig. 2b).^{35,46} This 180° switching of n also reverses the spin-splitting bands with CSVL²², and thereby reversing the first-order linear anomalous Hall responses.^{35,46} Using AHE as the readout method, electrical deterministic 180° switching of n has been achieved due to asymmetric energy barriers.³⁵ In contrast, as shown in Fig. 2c and 2c, under a strong H , canting m increases linearly with H (Note S1 in SI and Extended Data Fig. 2), which may further induce m -dependent Berry curvature that contributes to higher-order Hall responses. These four states (I–IV in Fig. 2a–d) are experimentally observed, producing a large MNLHE.

As shown in Fig. 2e, the black line depicts the Hall conductivity σ_H under strong magnetic field H up to approximately 60 T, measured at 93 K in the AM phase. Notably, this DC σ_H can be directly measured under DC longitudinal electric field. Three key features emerge: (1) For state I and II at weak H , a small kink-like offset σ_0 occurs near zero H , corresponding to the weak-field AHE from the 180° switching of n .³⁵ This offset, which does not increase with stronger H , is negligible compared to σ_H at 60 T, consistent with the alternating-sign Berry curvature at zero H . (2) For state III and IV at stronger H , σ_H deviates clearly from the OHE-induced linear σ_1H , and only a fit including both σ_2H^2 and σ_0 term works. σ_2H^2 term in DC measurements proves the existence of large MNLHE. (3) The σ_H curve for positive and negative H cannot be fitted by the same function, because both σ_2H^2 and σ_0 term change sign upon H reversal. This requires two non-analytic sign functions in the fitting function:

$\text{sgn}(H)\sigma_2H^2$ and $\text{sgn}(H)\sigma_0$. This non-analytic feature confirms that both $\text{sgn}(H)\sigma_2H^2$ and $\text{sgn}(H)\sigma_0$ term are relevant to first-order transitions upon H reversal, which is the 180° switching of magnetic structure in our case. The non-analytic feature is quite a distinctive characteristic of MNLHE, which is forbidden in traditional NLHE.

MNLHE is reproducible for Mn_5Si_3 across the range of temperatures within the AM phase (Fig. 3a). As the temperature increases from 93 to 200 K, the $\text{sgn}(H)\sigma_2H^2$ contribution gradually diminishes, which can be attributed to the temperature-sensitive Fermi-Dirac distribution, as discussed later. Meanwhile, $\text{sgn}(H)\sigma_0$ becomes less pronounced at higher temperatures, consistent with a reduction of AHE. In contrast, as shown in Fig. 3b, in the PM phase at 250 K, the $\text{sgn}(H)\sigma_2H^2$ dependence vanishes entirely, and a perfect linear and analytical dependence of σ_1H is observed, originated from the OHE. This result clearly excludes $\text{sgn}(H)\sigma_2H^2$ from non-magnetic scenarios (e.g. multi-carrier effects)⁴¹⁻⁴³ and undoubtedly correlates the appearance of $\text{sgn}(H)\sigma_2H^2$ with the magnetic order in the AM phase.

To further explore whether this $\text{sgn}(H)\sigma_H(H^2)$ term simply arises from an enhanced FM moment under strong H , we carried out control experiments on Mn_5Si_3 in the FM phase. The FM phase of Mn_5Si_3 is realized by growing thin film at room temperature, which lacks crystallinity while exhibits strong magnetism (Extended Data Fig. 3). As presented in Fig. 3c, besides $\text{sgn}(H)\sigma_0$ induced by 180° FM switching, σ_H increases linearly with H under strong field due to the OHE. This result confirms that the $\text{sgn}(H)\sigma_H(H^2)$ observed in the AM phase of Mn_5Si_3 thin film is not simply induced by a H -enhanced FM moment originating from possible magnetic impurities.

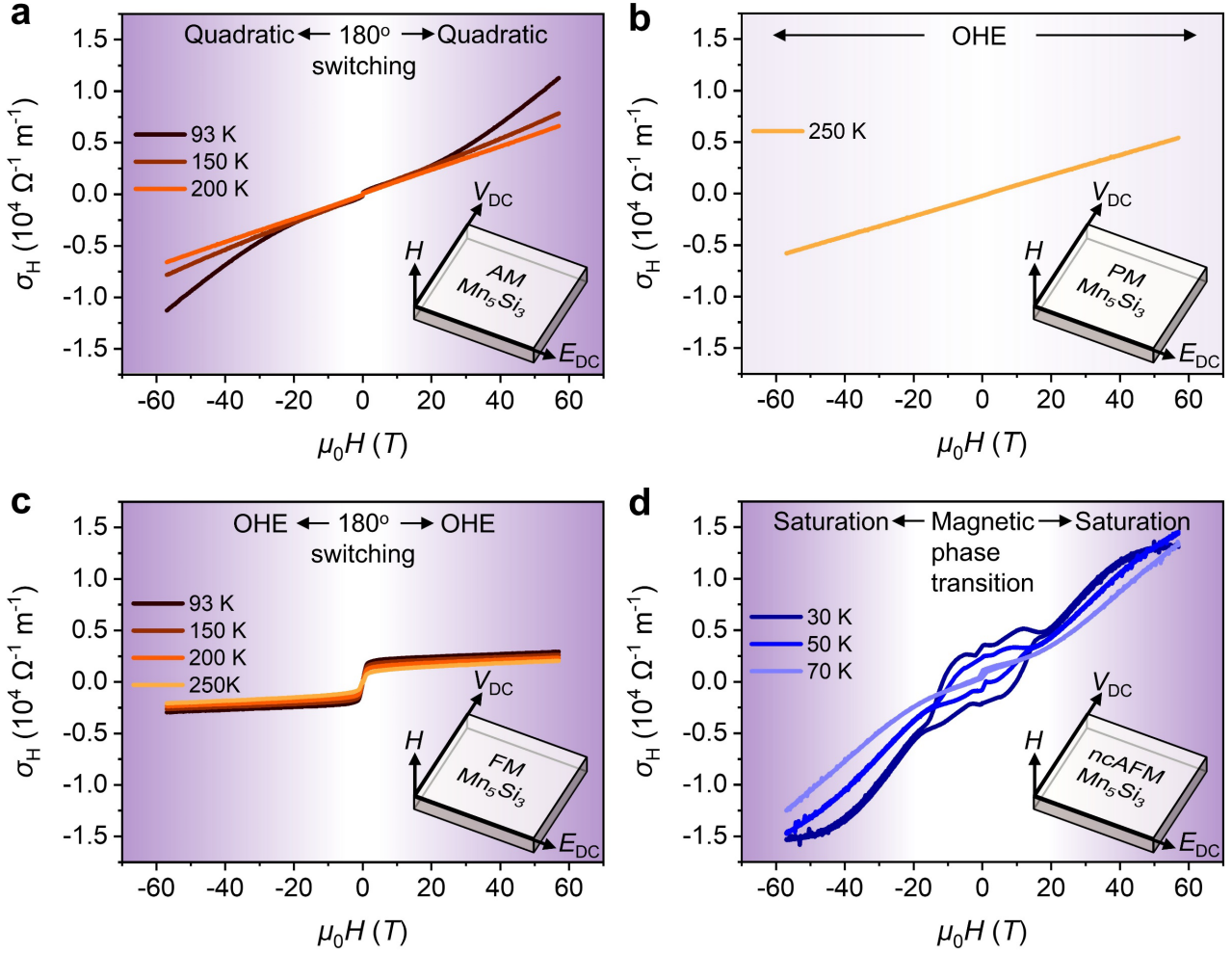


Figure 3 | Hall conductivity measurements under strong field for Mn_5Si_3 in different phases.

Temperature-dependent σ_H measured under perpendicular magnetic field for $Mn_5Si_3(0001)$ thin film at (a) the AM phase, (b) the PM phase, (c) the FM phase, and (d) the ncAFM phase.

Next, we prove that both Néel vector n and a tiny spontaneous canting moment m under zero field is crucial to generate this $\text{sgn}(H)\sigma_H(H^2)$ dependence. (1) To investigate the role of n , we carried out measurements in the ncAFM phase of Mn_5Si_3 thin film, as presented in Fig. 3d. The AHE-like hysteresis up to about 20 T is due to the magnetic phase transition triggered by H , consistent with previous works^{48,49} and beyond the scope of this work. Notably, under strong field, σ_H grows linearly with H for 70 K and 50 K, and even tends toward saturation at 30 K. These behaviors in the ncAFM phase are clearly distinct from those in the AM phase, revealing that simply AFM exchange coupling

in the ncAFM phase is insufficient to bring about the $\text{sgn}(H)\sigma_2 H^2$ dependence. The Néel vector n and corresponding specific magnetic structure in the AM phase plays an important role. (2) Secondly, the tiny spontaneous m is essential. With this m , the magnetic structure can be 180° switched by H , which reverses the hopping chirality (as discussed later) and results in the non-analytic characteristic of MNLHE. In contrast, if spontaneous m is strictly zero under zero H , even though a strong H can tilt n , n will not undergo a 180° switching. Consequently, the magnetic structure cannot be switched by 180° , which cannot lead to the non-analytic characteristic.

The exclusive appearance of non-analytic MNLHE in the AM phase of Mn_5Si_3 is reproducible, with the results in another Mn_5Si_3 thin film sample presented in Extended Data Fig. 4 as an example. Besides, the non-analytic MNLHE relies on the perpendicular alignment of the magnetic field H , electric field E_{DC} , and Hall voltage V_{DC} , as the σ_{H} is negligible when H is parallel to E_{DC} (Extended Data Fig. 5). As a result, supported by these comprehensive and consistent data provided above, we can confidently conclude that the non-analytic MNLHE in Mn_5Si_3 thin film is intrinsically originated in the response of the magnetic structure of AM under strong H .

Chiral next-nearest-neighbor hopping mechanism for MNLHE

We move on to explore the mechanism behind this non-analytic MNLHE. The key points are as follows. A tight-binding model of AM Mn_5Si_3 is built to derive the Hamiltonian, linking the change in band structure to H (Note S2 in SI). NNN hopping through magnetic atoms acquires additional exchange energy proportional to m , while also picks up a Haldane-like chiral flux phase⁵⁰ proportional to m . Together, these factors yield an m^2 term, ultimately producing the observed H^2 dependence in σ_{H} , as determined by the Berry curvature of the band structure (Note S3 in SI). Importantly, the magnetic structure can be 180° reversed by H , which switches the spin-splitting band and flips the hopping chirality, bringing about the non-analytic behavior. The details are below.

For simplicity without losing genericity, we build a 2D hexagonal lattice to represent Mn_5Si_3 unit

cell, as shown in Fig. 4a and Extended Data Fig. 6. A and B sites are located at the vertices of this lattice, formed by averaging the centroids of all non-magnetic atoms, including both Si and some Mn atoms. Four magnetic sites lie within this 2D plane, with the Néel vector n oriented along the y axis. In this model, the magnetic sublattices with antiferromagnetic coupling are connected by C_{2x} or $C_{2y}T$ symmetry, ensuring alternating-sign Berry curvatures at zero field. Meanwhile, PT and tT symmetry are broken. These are consistent with the magnetic structure of AM Mn_5Si_3 thin film. Hence, this model captures the essential symmetries of altermagnet Mn_5Si_3 while drastically simplifies the Hamiltonian.

Similar to the Haldane model for graphene⁵⁰ (Extended Data Fig. 7), both NN hopping t_1 and NNN hopping t_2 are considered, as denoted by black vectors in Fig. 4a. To ensure the final Hamiltonian analytically solvable, we focus on hopping between non-magnetic A and B sites, consistent with the two-band model of the band structure in AM.³⁰ This assumption is reasonable, as A and B sites account for most of the mass in the Mn_5Si_3 unit cell.

We then figure out all these NN and NNN hopping terms. The strong magnetic field H appears as an onsite energy term $-H\sigma_z$. For NN hopping between A and B, no magnetic atoms are involved, so the term simplifies to $t_1\sigma_0$. By contrast, for NNN hopping, the hopping paths encounter magnetic atoms (Fig. 4a), introducing exchange energy from the magnetic atoms. Hence, the NNN hopping term in the Hamiltonian is written as $-t_2 \sum_i (\mathbf{m}_i \cdot \boldsymbol{\sigma})$. Nevertheless, this term is proportional to m . It cannot explain the H^2 dependence of σ_H , which corresponds to a m^2 term.

Inspired by the Haldane model,⁵⁰ we consider the additional phase acquired during NNN hopping process, which may contribute to higher-order effects. Specifically, when an electron hops through a magnetic atom, spin-orbit coupling introduces an extra phase Φ . By combining conjugate relations, P symmetry, and M_yT symmetry (Note S2 in SI), there are only two independent phases, Φ_1 and Φ_2 , corresponding to hopping paths passing through two and one magnetic atom, respectively (Fig. 4b). We can prove that Φ_1 and Φ_2 are odd functions of m by analyzing time-reversal operation and M_z operation, meaning that, in the first-order approximation, Φ_1 and Φ_2 are linearly related to m (Note S2

in SI). Therefore, m^2 term emerges after considering both of this Haldane-like phase and the exchange energy as we introduced above, modifying $-t_2 \sum_i (\mathbf{m}_i \cdot \boldsymbol{\sigma})$ to $-t_2 e^{i\phi} \sum_i (\mathbf{m}_i \cdot \boldsymbol{\sigma})$.

Interestingly, under a strong positive H , the positive m constrains these phases in a clockwise hopping direction, forming chiral flux phases (Fig. 4b). Conversely, under a strong negative H , the negative m limits these phases in a counter-clockwise hopping chirality (Fig. 4c). It means that, the hopping chirality can be reversed by H , due to the 180° switching of m . This chiral hopping and its chirality reversal by H induce the non-analytic property of H^2 term in σ_H .

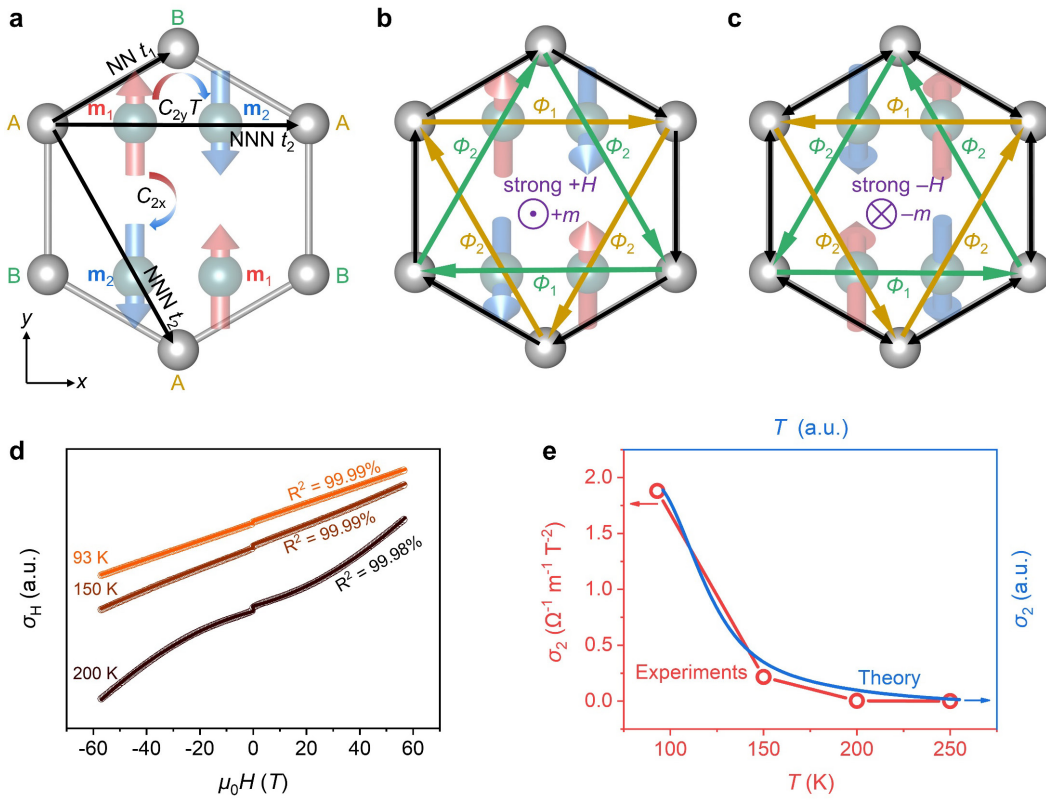


Figure 4 | Chiral next-nearest-neighbor hopping mechanism for the MNLHE. (a) 2D hexagonal lattice to model Mn_5Si_3 unit cell. The magnetic structure and Haldane-like NNN hopping phases of Mn_5Si_3 with (b) positive m under positive strong H , and (c) negative m under negative strong H . (d) Temperature dependent fitting results of experimental σ_H data by the theoretical model. (e) The experimental temperature dependence of σ_2 (left) and theoretical temperature dependence of σ_2 (right).

Finally, after some algebra analysis, the Hamiltonian is as follows (Note S2 in SI), which forms

the 2×2 Hamiltonian of $\begin{bmatrix} \mathcal{H}_{K_{\pm}}^{\uparrow} & 0 \\ 0 & \mathcal{H}_{K_{\pm}}^{\downarrow} \end{bmatrix}$ presented below.

$$\mathcal{H}_{K_{\pm}}^{\uparrow} = -H\tau_0 \pm k_x\tau_x + k_y\tau_y \pm m^2\tau_z \quad (1)$$

$$\mathcal{H}_{K_{\pm}}^{\downarrow} = +H\tau_0 \pm k_x\tau_x + k_y\tau_y \mp m^2\tau_z \quad (2)$$

Remarkably, Eq. (1-2) is very similar with the Hamiltonian of graphene, except for the $m^2\tau_z$ term. This $m^2\tau_z$ term opens the gap of the Dirac cones for the emergence of additional Berry curvature under magnetic field, which gives the final form of Hall conductivity as following Eq. (3) (Note S3 in SI):

$$\sigma_H \cong \text{sgn}(H) \sigma_0 + \sigma_1 H + \text{sgn}(H) \sigma_2 H^2 \quad (3)$$

The sign functions in the Eq. (3) bring about the non-analytic feature in MNLHE. The 180° switching of n changes the sign of the anomalous Hall conductivity, described by the $\text{sgn}(H)\sigma_0$ term, while, the 180° switching of m reverses the chirality of hopping, contributing to $\text{sgn}(H)\sigma_2 H^2$.

Figure 4d shows the fitting results of our experimental data using Eq. (3). The model agrees well with the experimental measurements, with R^2 values exceeding 99.98% across different temperatures. The fitted σ_2 values, summarized in Fig. 4e, increases with decreasing temperatures. Because the intrinsic anomalous Hall conductivity is originated from the integral of Berry curvatures multiplied by Fermi-Dirac distribution, this temperature dependence of σ_2 reflects how the Fermi-Dirac distribution influences the band occupation. Considering the influence of temperature on the Fermi-Dirac distribution, this temperature dependence of σ_2 can also be well captured theoretically (Fig. 4e).

Discussions

We discuss the requirements for the non-analytic MNLHE here. Alternating-sign Berry curvature instead of single-sign Berry curvature is vital to prevent the higher-order H -dependence from being

overshadowed by the first-order effect, thus excluding FMs, as confirmed by control experiments on FM Mn_5Si_3 (Fig. 3c). Moreover, the non-analytic feature requires a tiny spontaneous canting moment, which can be switched by 180° upon H reversal to flip the hopping chirality. This excludes bulk collinear AFM Mn_5Si_3 , as its PT and tT symmetry forbid spontaneous net canting moment. In fact, the specific H^2 dependence from the m^2 term is due to the exchange interactions and Haldane-like hopping phases, which is dependent on the unique crystal and magnetic structure of Mn_5Si_3 thin film in the AM phase. Hence, while other magnets with antiferromagnetically coupled moments and tiny spontaneous canting could exhibit MNLHE, the H^2 dependence may not appear. ncAFM Mn_5Si_3 is a good example, where its complex non-coplanar magnetic structure⁴⁵ influences the detail of magnetic exchange and Haldane-like hopping phases, and thus does not bring about H^2 dependence (Fig. 3d). As a result, the MNLHE with non-analytic H^2 dependence is a fingerprint of AM Mn_5Si_3 , which cannot be observed in FM Mn_5Si_3 , collinear AFM or ncAFM Mn_5Si_3 .

In summary, a large MNLHE, characterized by a non-analytic $\sigma_2 H^2$ term that does not saturate under 60 T, is experimentally observed via DC Hall measurements and theoretically comprehended by chiral NNN hopping mechanism. MNLHE emerges exclusively in the AM phase, while absence in other phases of Mn_5Si_3 , thereby excluding possible multicarrier artifacts and highlighting the crucial role of the interplay between H and altermagnetism. The H^2 dependence originates from the m^2 NNN hopping term in the Hamiltonian: one m from exchange interaction, and the other m from a Haldane-like chiral flux phase. This m^2 term opens a gap in the spin-splitting bands of AMs with CSVL, with band shift due to Zeeman effect affecting the Berry curvature near the Fermi surface, which ultimately brings about H^2 dependence. The non-analytic feature, unique in MNLHE and absent in ENLHE, is determined by the hopping chirality, which reverses as H changes sign and flips the magnetic structure

and spin-splitting bands. This MNLHE, involving higher-order dependence of σ_H with H , can in principle occur in any magnetic material with alternating-sign Berry curvature and tiny spontaneous canting—conditions well met by some other AMs like MnTe and CrSb. Our findings on MNLHE not only deepen the fundamental understanding of fingerprints in altermagnet Mn₅Si₃ and its spin-splitting band structure, but also hold promise in pulsed high-field sensing technologies, supporting both scientific researches and engineering applications.

References

- 1 Hall, E. H. On a new action of the magnet on electric currents. *Am. J. Math.* **2**, 287-292 (1879).
- 2 Klitzing, K. v., Dorda, G. & Pepper, M. New Method for High-Accuracy Determination of the Fine-Structure Constant Based on Quantized Hall Resistance. *Phys. Rev. Lett.* **45**, 494-497 (1980).
- 3 Tsui, D. C., Stormer, H. L. & Gossard, A. C. Two-Dimensional Magnetotransport in the Extreme Quantum Limit. *Phys. Rev. Lett.* **48**, 1559-1562 (1982).
- 4 Bernevig, B. A., Hughes, T. L. & Zhang, S.-C. Quantum Spin Hall Effect and Topological Phase Transition in HgTe Quantum Wells. *Science* **314**, 1757-1761 (2006).
- 5 Chang, C.-Z. *et al.* Experimental Observation of the Quantum Anomalous Hall Effect in a Magnetic Topological Insulator. *Science* **340**, 167-170 (2013).
- 6 Kato, Y. K., Myers, R. C., Gossard, A. C. & Awschalom, D. D. Observation of the Spin Hall Effect in Semiconductors. *Science* **306**, 1910-1913 (2004).
- 7 Nagaosa, N., Sinova, J., Onoda, S., MacDonald, A. H. & Ong, N. P. Anomalous Hall effect. *Rev. Mod. Phys.* **82**, 1539-1592 (2010).
- 8 Sodemann, I. & Fu, L. Quantum Nonlinear Hall Effect Induced by Berry Curvature Dipole in Time-Reversal Invariant Materials. *Phys. Rev. Lett.* **115**, 216806 (2015).
- 9 Ma, Q. *et al.* Observation of the nonlinear Hall effect under time-reversal-symmetric conditions. *Nature* **565**, 337-342 (2019).
- 10 Kang, K., Li, T., Sohn, E., Shan, J. & Mak, K. F. Nonlinear anomalous Hall effect in few-layer WTe₂. *Nat. Mater.* **18**, 324-328 (2019).
- 11 Xiao, J. *et al.* Berry curvature memory through electrically driven stacking transitions. *Nat. Phys.* **16**, 1028-1034 (2020).
- 12 Ho, S.-C. *et al.* Hall effects in artificially corrugated bilayer graphene without breaking time-reversal symmetry. *Nat. Electron.* **4**, 116-125 (2021).
- 13 Lai, S. *et al.* Third-order nonlinear Hall effect induced by the Berry-connection polarizability tensor. *Nat. Nanotechnol.* **16**, 869-873 (2021).
- 14 He, P. *et al.* Third-order nonlinear Hall effect in a quantum Hall system. *Nat. Nanotechnol.* **19**, 1460-1465 (2024).
- 15 He, Z. & Weng, H. Giant nonlinear Hall effect in twisted bilayer WTe₂. *npj Quantum Mater.* **6**, 101 (2021).

- 16 Huang, M. Z. *et al.* Intrinsic Nonlinear Hall Effect and Gate-Switchable Berry Curvature Sliding in Twisted Bilayer Graphene. *Phys. Rev. Lett.* **131**, 066301 (2023).
- 17 Kumar, D. *et al.* Room-temperature nonlinear Hall effect and wireless radiofrequency rectification in Weyl semimetal TaIrTe₄. *Nat. Nanotechnol.* **16**, 421-425 (2021).
- 18 Zhao, T.-Y. *et al.* Gate-Tunable Berry Curvature Dipole Polarizability in Dirac Semimetal Cd₃As₂. *Phys. Rev. Lett.* **131**, 186302 (2023).
- 19 Min, L. *et al.* Strong room-temperature bulk nonlinear Hall effect in a spin-valley locked Dirac material. *Nat. Commun.* **14**, 364 (2023).
- 20 Lee, J.-E. *et al.* Spin-orbit-splitting-driven nonlinear Hall effect in NbIrTe₄. *Nat. Commun.* **15**, 3971 (2024).
- 21 Han, J. *et al.* Room-temperature flexible manipulation of the quantum-metric structure in a topological chiral antiferromagnet. *Nat. Phys.* **20**, 1110-1117 (2024).
- 22 Ma, H. Y. *et al.* Multifunctional antiferromagnetic materials with giant piezomagnetism and noncollinear spin current. *Nat. Commun.* **12**, 2846 (2021).
- 23 Zhang, C.-P., Gao, X.-J., Xie, Y.-M., Po, H. C. & Law, K. T. Higher-order nonlinear anomalous Hall effects induced by Berry curvature multipoles. *Phys. Rev. B* **107**, 115142 (2023).
- 24 Sankar, S. *et al.* Experimental Evidence for a Berry Curvature Quadrupole in an Antiferromagnet. *Phys. Rev. X* **14**, 021046 (2024).
- 25 Du, Z. Z., Lu, H.-Z. & Xie, X. C. Nonlinear Hall effects. *Nat. Rev. Phys.* **3**, 744-752 (2021).
- 26 Gao, Y., Yang, S. A. & Niu, Q. Field Induced Positional Shift of Bloch Electrons and Its Dynamical Implications. *Phys. Rev. Lett.* **112**, 166601 (2014).
- 27 He, P. *et al.* Bilinear magnetoelectric resistance as a probe of three-dimensional spin texture in topological surface states. *Nat. Phys.* **14**, 495-499 (2018).
- 28 Kim, D.-J. *et al.* Spin Hall-induced bilinear magnetoelectric resistance. *Nat. Mater.* **23**, 1509-1514 (2024).
- 29 Šmejkal, L., Sinova, J. & Jungwirth, T. Beyond Conventional Ferromagnetism and Antiferromagnetism: A Phase with Nonrelativistic Spin and Crystal Rotation Symmetry. *Phys. Rev. X* **12**, 031042 (2022).
- 30 Šmejkal, L., Sinova, J. & Jungwirth, T. Emerging Research Landscape of Altermagnetism. *Phys. Rev. X* **12**, 040501 (2022).
- 31 Amin, O. J. *et al.* Nanoscale imaging and control of altermagnetism in MnTe. *Nature* **636**, 348-353 (2024).
- 32 Krempaský, J. *et al.* Altermagnetic lifting of Kramers spin degeneracy. *Nature* **626**, 517-522 (2024).
- 33 Feng, Z. *et al.* An anomalous Hall effect in altermagnetic ruthenium dioxide. *Nat. Electron.* **5**, 735-743 (2022).
- 34 Gonzalez Betancourt, R. D. *et al.* Spontaneous Anomalous Hall Effect Arising from an Unconventional Compensated Magnetic Phase in a Semiconductor. *Phys. Rev. Lett.* **130**, 036702 (2023).
- 35 Han, L. *et al.* Electrical 180° switching of Néel vector in spin-splitting antiferromagnet. *Sci. Adv.* **10**, eadn0479 (2024).
- 36 Reichlova, H. *et al.* Observation of a spontaneous anomalous Hall response in the Mn₅Si₃ d-wave altermagnet candidate. *Nat. Commun.* **15**, 4961 (2024).
- 37 Zhou, Z. *et al.* Crystal design of altermagnetism. *arXiv:2403.07396* (2024).

- 38 Cheong, S.-W. & Huang, F.-T. Altermagnetism with non-collinear spins. *npj Quantum Mater.* **9**, 13 (2024).
- 39 Fang, Y., Cano, J. & Ghorashi, S. A. A. Quantum Geometry Induced Nonlinear Transport in Altermagnets. *Phys. Rev. Lett.* **133**, 106701 (2024).
- 40 Leiviskä, M. *et al.* Anisotropy of the anomalous Hall effect in thin films of the altermagnet candidate Mn₅Si₃. *Phys. Rev. B* **109**, 224430 (2024).
- 41 Urata, T., Hattori, W. & Ikuta, H. High mobility charge transport in a multicarrier altermagnet CrSb. *Phys. Rev. Mater.* **8**, 084412 (2024).
- 42 Bai, Y. *et al.* Nonlinear field dependence of Hall effect and high-mobility multi-carrier transport in an altermagnet CrSb. *Appl. Phys. Lett.* **126**, 042402 (2025).
- 43 Peng, X. *et al.* Scaling Behavior of Magnetoresistance and Hall Resistivity in Altermagnet CrSb. *arXiv:2412.12263* (2024).
- 44 Brown, P. & Forsyth, J. Antiferromagnetism in Mn₅Si₃: the magnetic structure of the AF2 phase at 70 K. *J. Phys. Condens. Matter* **7**, 7619 (1995).
- 45 Sürgers, C., Fischer, G., Winkel, P. & Löhneysen, H. V. Large topological Hall effect in the non-collinear phase of an antiferromagnet. *Nat. Commun.* **5**, 3400, doi:10.1038/ncomms4400 (2014).
- 46 Han, L. *et al.* Observation of non-volatile anomalous Nernst effect in altermagnet with collinear Néel vector. *arXiv:2403.13427* (2024).
- 47 Badura, A. *et al.* Observation of the anomalous Nernst effect in altermagnetic candidate Mn₅Si₃. *arXiv:2403.12929* (2024).
- 48 Sürgers, C. *et al.* Switching of a large anomalous Hall effect between metamagnetic phases of a non-collinear antiferromagnet. *Sci. Rep.* **7**, 42982 (2017).
- 49 Sürgers, C., Kittler, W., Wolf, T. & Löhneysen, H. v. Anomalous Hall effect in the noncollinear antiferromagnet Mn₅Si₃. *AIP Adv.* **6**, 055604 (2016).
- 50 Haldane, F. D. M. Model for a Quantum Hall Effect without Landau Levels: Condensed-Matter Realization of the "Parity Anomaly". *Phys. Rev. Lett.* **61**, 2015-2018 (1988).
- 51 Evans, R. F. L. *et al.* Atomistic spin model simulations of magnetic nanomaterials. *J. Phys. Condens. Matter* **26**, 103202 (2014).
- 52 dos Santos, F. J. *et al.* Spin waves in the collinear antiferromagnetic phase of Mn₅Si₃. *Phys. Rev. B* **103**, 024407 (2021).

Methods

Sample preparation. 100 nm Mn₅Si₃(0001) films were grown on Al₂O₃(0001) substrate by co-sputtering of Mn and Si at 600 °C with a rate of 0.4 Å s⁻¹ under a base pressure below 5 × 10⁻⁸ Torr. For pulsed high field measurements, 0.15 mm × 0.15 mm square Cr(10 nm)/Au(80 nm) electrodes were deposited for connection by Au wire and silver conductive paste. All the samples were kept in a glove box with O₂ and H₂O < 0.01 parts per million to prevent degradation or oxidation.

Characterizations. Cross-sectional high-angle annular dark-field scanning transmission electron microscopy (HAADF-STEM) was conducted on an FEI Titan 80-300 electron microscopy equipped with a monochromator unit, a probe spherical aberration corrector, a post-column energy filter system (Gatan Tridiem 865 ER), and a Gatan 2k slow scan CCD system, operating at 300 kV, combining an energy resolution of ~ 0.6 eV and a dispersion of 0.2 eV per channel with a spatial resolution of ~ 0.08 nm. The longitudinal resistivity and anomalous Hall resistivity of Mn_5Si_3 films were measured using commercial Physical Property Measurement System (PPMS, Quantum Design). Magnetic hysteresis curves were collected for $5\text{ mm} \times 3\text{ mm} \times 100\text{ nm}$ $\text{Mn}_5\text{Si}_3(0001)$ thin films on 0.5 mm -thick $\text{Al}_2\text{O}_3(0001)$ substrate under out-of-plane magnetic field, using a commercial superconducting quantum interference device (SQUID, MPMS3), where the diamagnetic contribution of substrate was subtracted.

Tight binding model calculations. The tight-binding model was based on the 2D hexagonal lattice with two nonmagnetic sites and four magnetic sites in one cell. The bases were chosen as the two nonmagnetic sites with two spin degrees of freedom, while the magnetic atoms influence the hopping terms. The low-energy approximation was applied that Hamiltonian can be decomposed into two 2×2 matrices. The intrinsic anomalous Hall conductivity can be analytically calculated from the integral of Berry curvatures on occupied states.

Atomic spin simulations. Atomic spin simulations were carried out on VAMPIRE software,⁵¹ which can define specific lattice parameters a and c consistent with our experimental values for Mn_5Si_3 thin film.⁴⁶ Four exchange interactions were considered, namely $J_1 = -12.23$ meV, $J_2 = -2.16$ meV, $J_3 = 3.98$ meV, and $J_4 = 2.89$ meV, with magnitude consistent with former DFT calculations.^{35,52} The DMI vector was set along x axis with a magnitude of 1.35 meV.³⁵

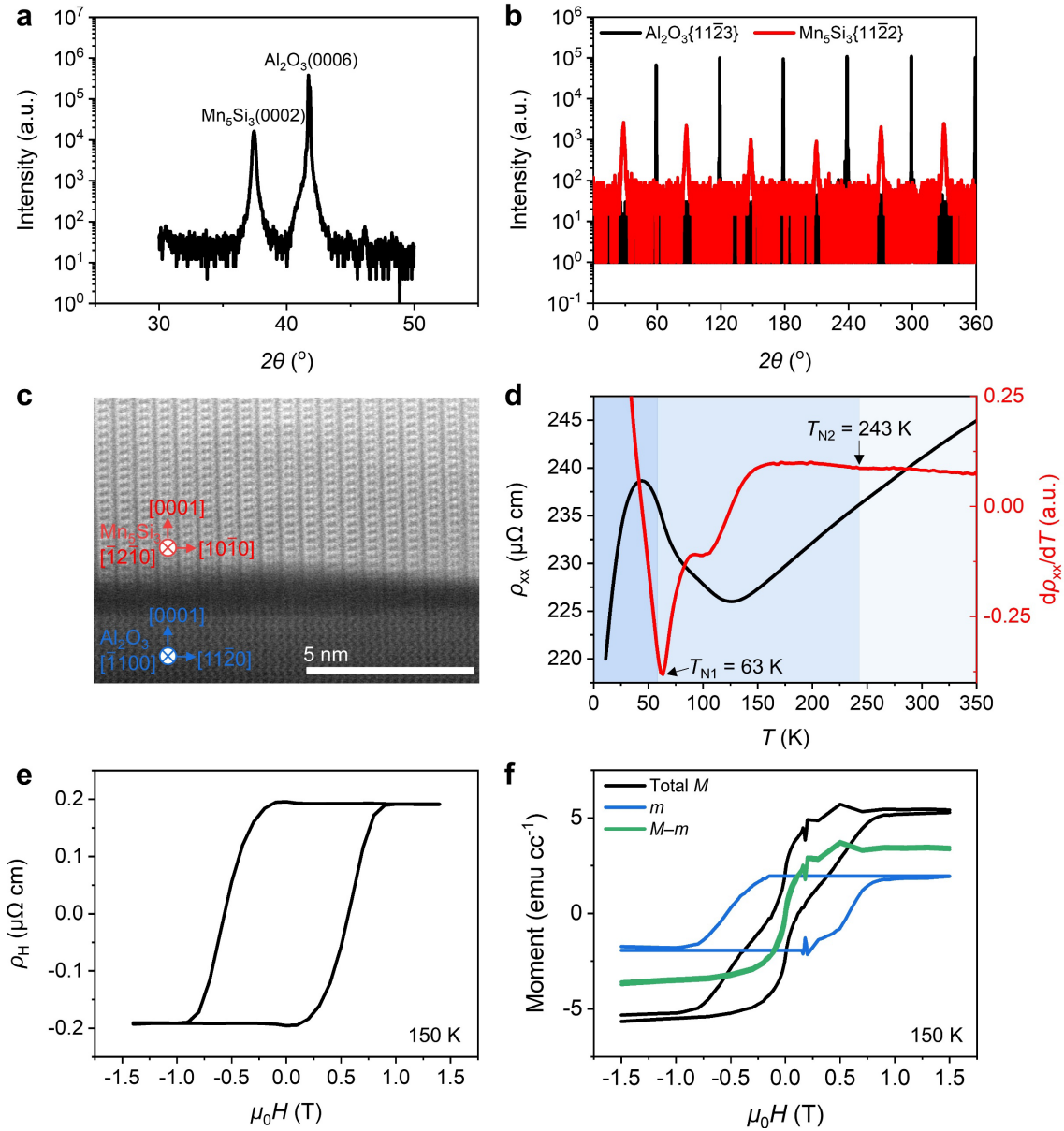
Data availability. All data needed to evaluate the conclusions in the paper are present in the paper

and/or the Supplementary Materials.

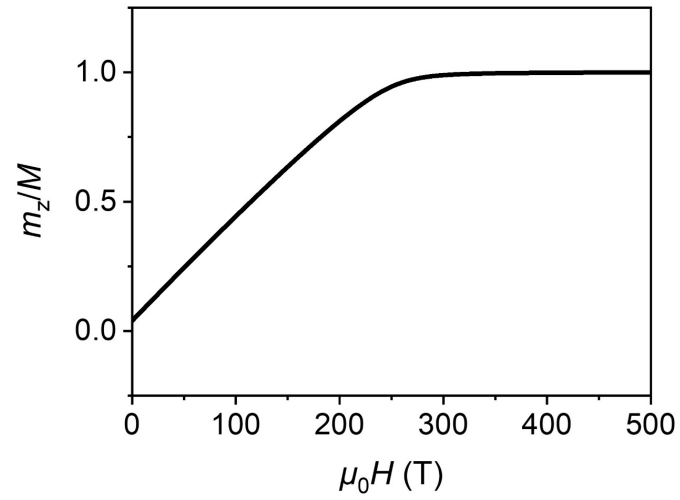
Acknowledgements. This work was supported by the National Key R&D Program of China (grant nos. 2021YFA1401500 and 2022YFA1402603), National Natural Science Foundation of China (grant nos. 52225106, 12241404), and Hong Kong Research Grants Council (grant nos. 16303821, 16306722, and 16304523).

Author contributions. L. H., C. S. and F. P. proposed the ideas and designed the experiments. X. F. and J. L. carried out theoretical analysis and calculations. L. H., Y. Z., and X. L. performed pulsed high field measurements. This work was conceived, led, coordinated and guided by C. S., J. L. and F. P. All the authors contributed to the writing of the manuscript.

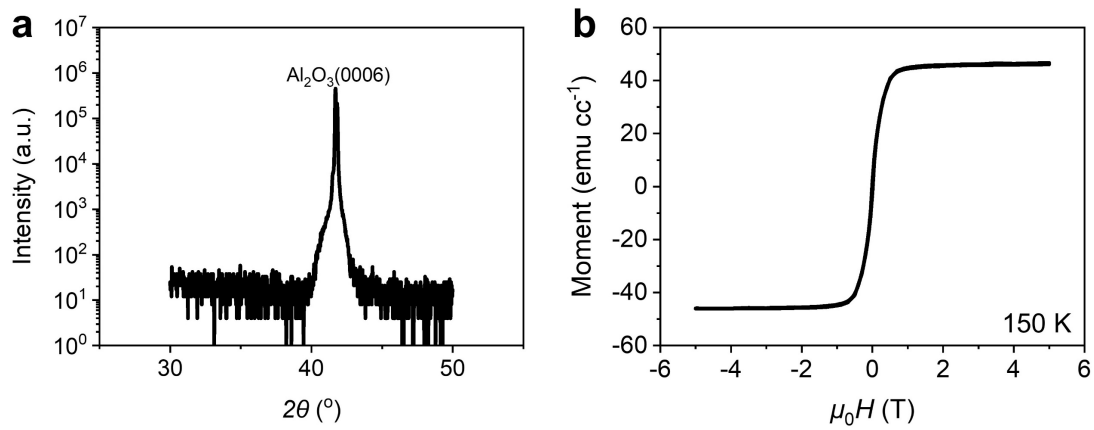
Competing interests. The authors declare no competing interests.



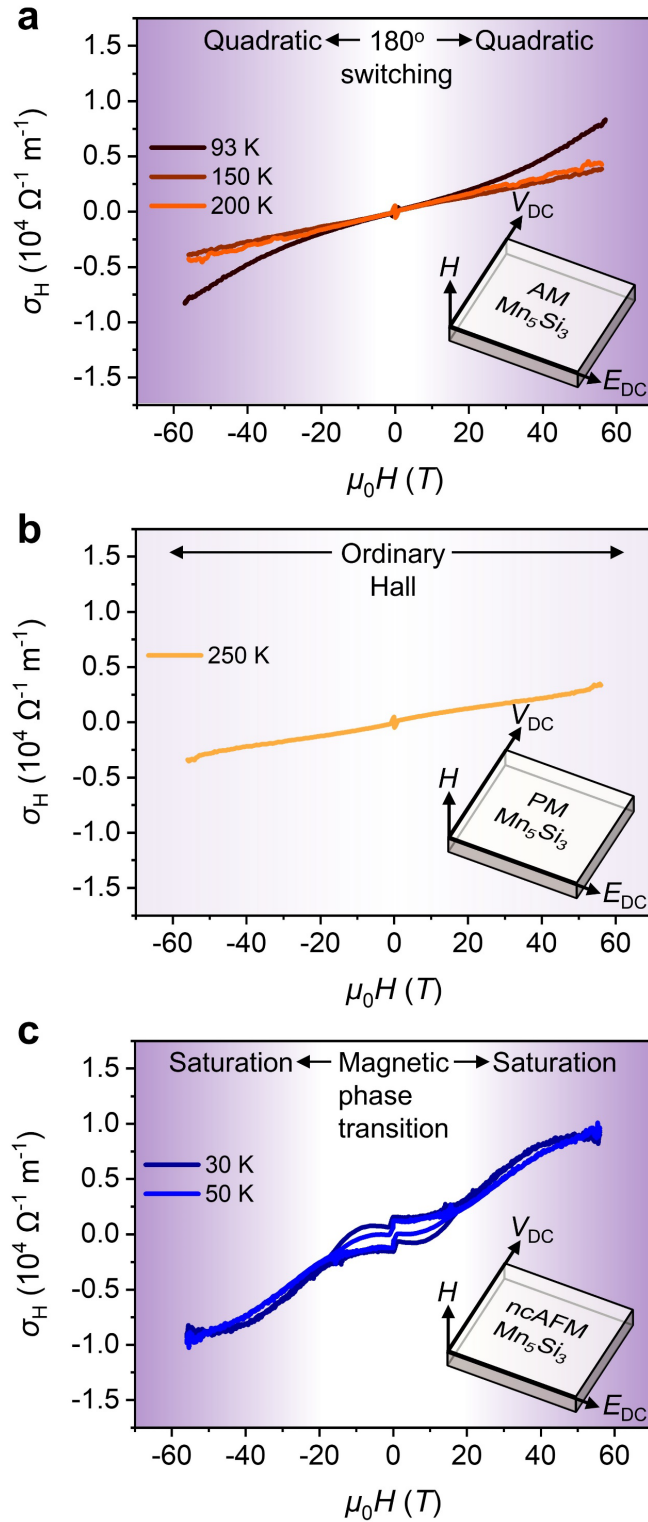
Extended Data Fig. 1 | Basic characterizations of the Mn₅Si₃ thin film. (a) X-ray diffraction spectrum of Mn₅Si₃(0001) thin film. (b) ϕ -scan X-ray diffraction measurements for Al₂O₃(0001)/Mn₅Si₃(0001). An in-plane 30°-shifted growth mode is confirmed from the 30° shift between Mn₅Si₃{11 $\bar{2}$ 2} and Al₂O₃{11 $\bar{2}$ 3} peaks. (c) HAADF-STEM image of Al₂O₃(0001)/Mn₅Si₃(0001) under zone axis of Al₂O₃< $\bar{1}$ 100>. (d) Temperature-dependent longitudinal resistivity ρ with temperature T (black line) and its temperature derivative (red line). (e) Hysteresis of anomalous Hall resistivity ρ_H and (f) total M , canting moment m and defect-induced $M-m$ measured at 150 K. For ρ_H , a field-linear background was removed.



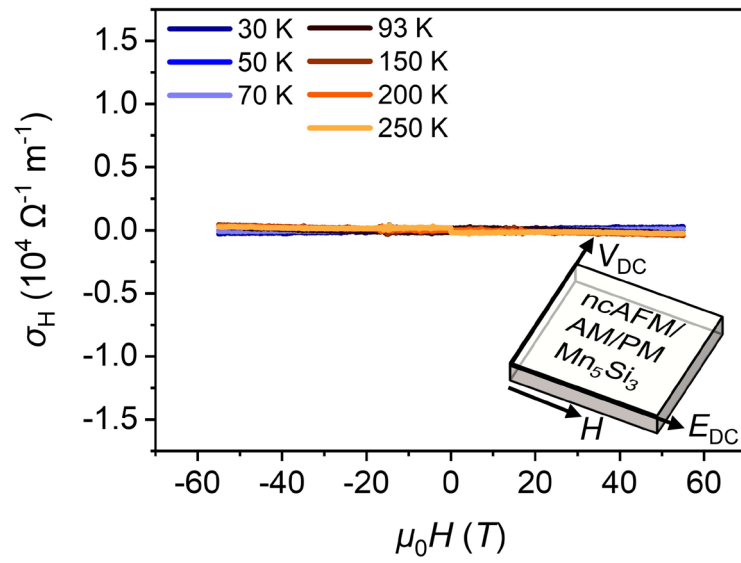
Extended Data Fig. 2 | Canting m along z direction under strong out-of-plane magnetic field H for AM phase of Mn_5Si_3 , calculated by atomic spin simulations.



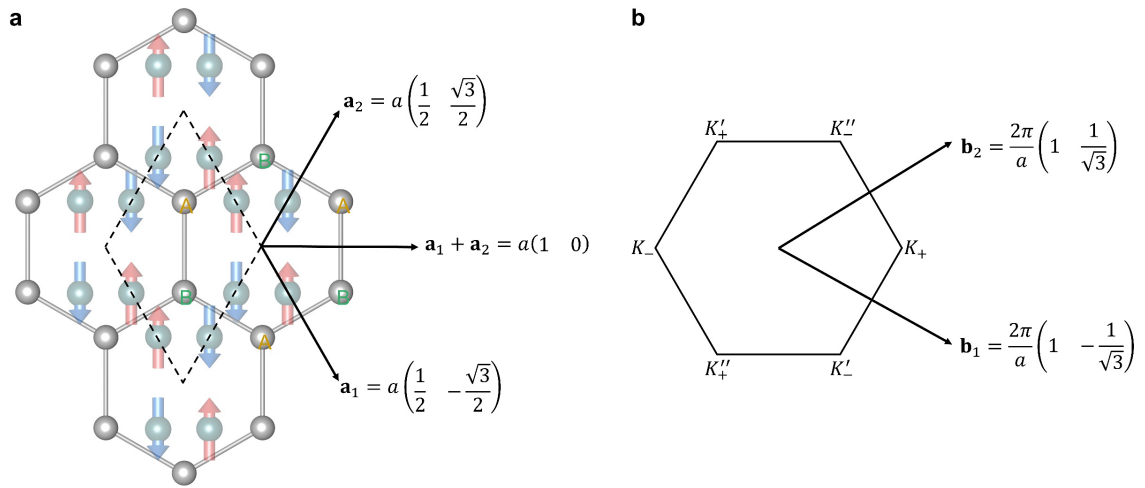
Extended Data Fig. 3 | Characterizations of the ferromagnetic Mn_5Si_3 thin film. (a) X-ray diffraction spectrum. (b) Magnetic hysteresis measured at 150 K.



Extended Data Fig. 4 | Temperature dependent measurements of MNLHE on another Mn_5Si_3 thin film sample. σ_H measured under perpendicular magnetic field for $Mn_5Si_3(0001)$ thin film at (a) the AM phase, (b) the PM phase, and (c) the ncAFM phase.

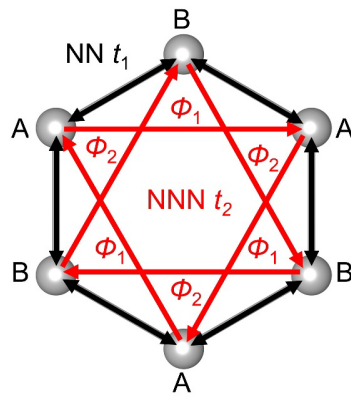


Extended Data Fig. 5 | Temperature dependent Hall conductivity measured with parallel configuration of magnetic field and electric field.

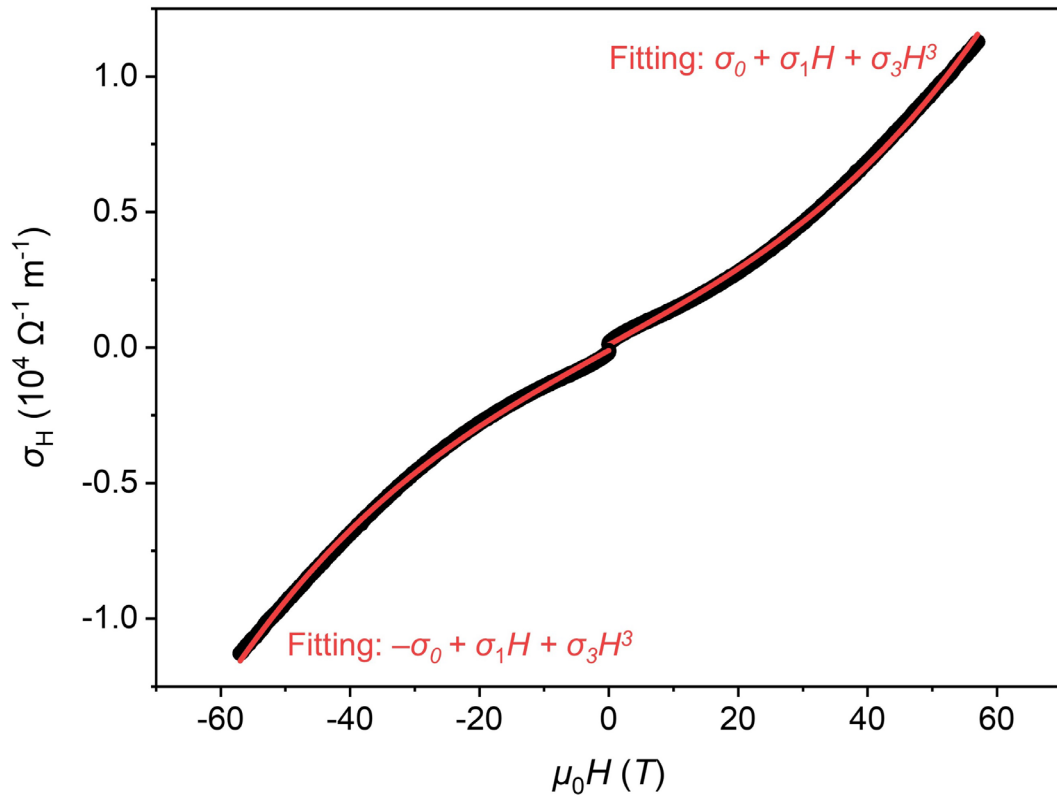


Extended Data Fig. 6 | Schematic of the 2D hexagonal lattice in (a) real space and (b) reciprocal space.

Graphene: Haldane model



Extended Data Fig. 7 | Schematic of the Haldane model in graphene.



Extended Data Fig. 8 | Fitting of the Hall conductivity at 93 K by considering an analytic $\sigma_3(H^3)$ term instead of the non-analytic $\text{sgn}(H)\sigma_2 H^2$ term.